Disorder-driven fast Na^+ transport: From crystalline to amorphous networks in the mixed-anion $NaTaO_xCl_{6-2x}$ oxychlorides

Justin Leifeld, Abigail C. Parsons, Alexandra Morscher, Xabier Martinez de Irujo-Labalde, Marvin A. Kraft, Oskar G. Soulas, Bibek Samanta, Wiebke Zielasko, Neelam Yadav, Kyra Strotmann, Niina Jalarvo, Bruno V. M. Rodrigues, Adam Slabon, Philipp Adelhelm, Michael Ryan Hansen, David O. Scanlon, Wolfgang G. Zeier, Alexander G. Squires**

Solid electrolytes are central to enabling safe, high-energy solid-state sodium batteries. While oxyhalide type conductors have rapidly advanced lithium-based systems, their sodium analogues remain less understood and underdeveloped. This gap arises from their intrinsically amorphous nature, which obscures structure–transport relationships and limits rational design. Here, we elucidate the atomic-scale origins of sodium-ion conduction in the mixed-anion series $NaTaO_xCl_{6-2x}$ using a combination of experimental and computational approaches. We reveal that composition-dependent, disordered yet extended chain motifs emerge as key structural units governing ion mobility. By tuning chain connectivity, we achieve a high ionic conductivity of ~4.0 $mS \cdot cm^{-1}$ and a corresponding self-diffusion coefficient of $6.6 – 8.2 \times 10^{-11}$ $m^2 \cdot s^{-1}$, ranking among to the fastest reported for sodium oxyhalides. These findings establish clear structure–property correlations in amorphous superionic conductors and provide a blueprint for the targeted design of next-generation solid electrolytes for sodium solid-state batteries.

Electrification of energy systems hinges on scalable and cost-effective storage technologies.[1] Sodium solid-state batteries (SSSBs) offer a sustainable alternative to lithium-based systems owing to the abundance and low cost of sodium.[2],[3],[4] Their progress, however, remains limited by the lack of solid electrolytes that simultaneously combine high ionic conductivity, wide electrochemical stability, and good electrode compatibility.[5],[6]

Mixed-anion oxyhalides have recently emerged as a versatile design platform for solid electrolytes. In lithium systems such as $Li_{1-x}NbO_{1-x}Cl_{4+x}$,[7] partial substitution of halide ions with O^{2-} enhances ionic conductivity and oxidative stability by introducing local structural distortions and softening the diffusion landscape. Comparable strategies in sodium oxyhalides, including $NaNbO_xCl_{6-2x}$,[8] have yielded conductivities typically below 1 $mS \cdot cm^{-1}$, indicating that most Na-based frameworks remain too rigid for fast ion motion. A comparison of reported ionic conductivities of sodium oxyhalide electrolytes is provided in Table S1 in the Supporting Information.

Among these chemistries, tantalum-based oxyhalides stand out as particularly promising. Crystalline perovskite-related $NaTaCl_6$ exhibits modest ionic conductivity ($2.8 - 5.2 \times 10^{-2}$ $mS \cdot cm^{-1}$)[9],[10]. Amorphous $NaTaCl_6$ shows impressive ionic conductivity (4 $mS \cdot cm^{-1}$), however, to achieve amorphization intensive ball-milling over long reaction times is required.[11] Oxygen incorporation yields amorphous $NaTaOCl_4$ with a conductivity (~1.5 $mS \cdot cm^{-1}$) without the requirement for energy intensive synthesis.[12],[13] However, the origin of this enhancement remains unclear, as oxygen incorporation leads to a loss of long-range order that hinders conventional structure–property analyses. Previous studies have speculated that oxygen may either form bi-$[TaCl_xO_{6-x}]^{(7-x)-}$ units or act as a bridging atom that connecting adjacent $[TaCl_6]^-$ octahedra.[12],[14] A deeper understanding of the resulting structural motifs is still lacking, limiting rational material design.

In this work, we use experiment and computation to uncover how oxide-ion incorporation governs structure and ion transport in the mixed-anion series $NaTaO_xCl_{6-2x}$ ($0 \leq x \leq 1$). Combining structural characterization, electrochemical measurements, and atomistic simulations, we resolve the local structural environments that underpin Na^+ mobility. Data-driven analyses reveal how oxide substitution induces distinct short-range order and establishes clear correlations between dynamic disorder and ionic conductivity. We demonstrate the feasibility of these materials as catholytes in sodium solid-state batteries. These findings provide a unified picture of structure–transport relationships in disordered sodium oxyhalides and highlight mixed-anion design as a powerful strategy for next-generation solid-state electrolytes.

MAIN TEXT

Structural evolution across the $NaTaO_xCl_{6-2x}$ series. The $NaTaO_xCl_{6-2x}$ series, prepared for $x = 0 – 1$ in increments of 0.125, was mechanochemically synthesized and characterized using complementary average- and local-structure probes. The reported compositions correspond to the nominal stoichiometric ratios that are used during synthesis. X-ray diffraction (XRD) reveals a progressive loss of crystallinity with increasing oxygen incorporation (Figure S1a). For compositions with lower oxygen content ($x \leq 0.375$), sharp Bragg reflections indicate long-range order and the coexistence of two phases, with the crystalline phase consistent with monoclinic $NaTaCl_6$ ($P2_1/n$, ICSD #36519). With higher oxygen content, the reflections broaden, especially around $q \approx 1$ Å^{-1}, signaling structural disorder. At $x = 0.5$, the pattern becomes dominated by broad diffuse features, and for $x \geq 0.5$, two amorphous humps centered at $q \approx 1.0$ and 1.6 Å^{-1} dominate, evidencing the collapse of long-range periodicity with the O^{2-} incorporation. Quantitative phase analysis using LaB_6 as an internal standard (Figures S1b, S2, Table S2) confirms a near-linear decrease of the crystalline phase, which is identified as $NaTaCl_6$, from ~90 wt.% at $x = 0.0$ to 0 wt.% at $x = 0.5$. The disappearance of crystalline side phases and the absence of detectable precursors further indicate that the mechanochemical reaction proceed to completion. These observations support that the nominal compositions used in this work reasonably reflect the effective oxygen incorporation. Overall, these results show that the oxygen substitution destabilizes the halide framework, driving a transition to a disordered, glass-like structure that persists at high oxygen content. However, the structural differences among the amorphous compositions ($x \geq 0.5$) cannot be resolved by diffraction alone, motivating simulation and complementary experimental techniques.

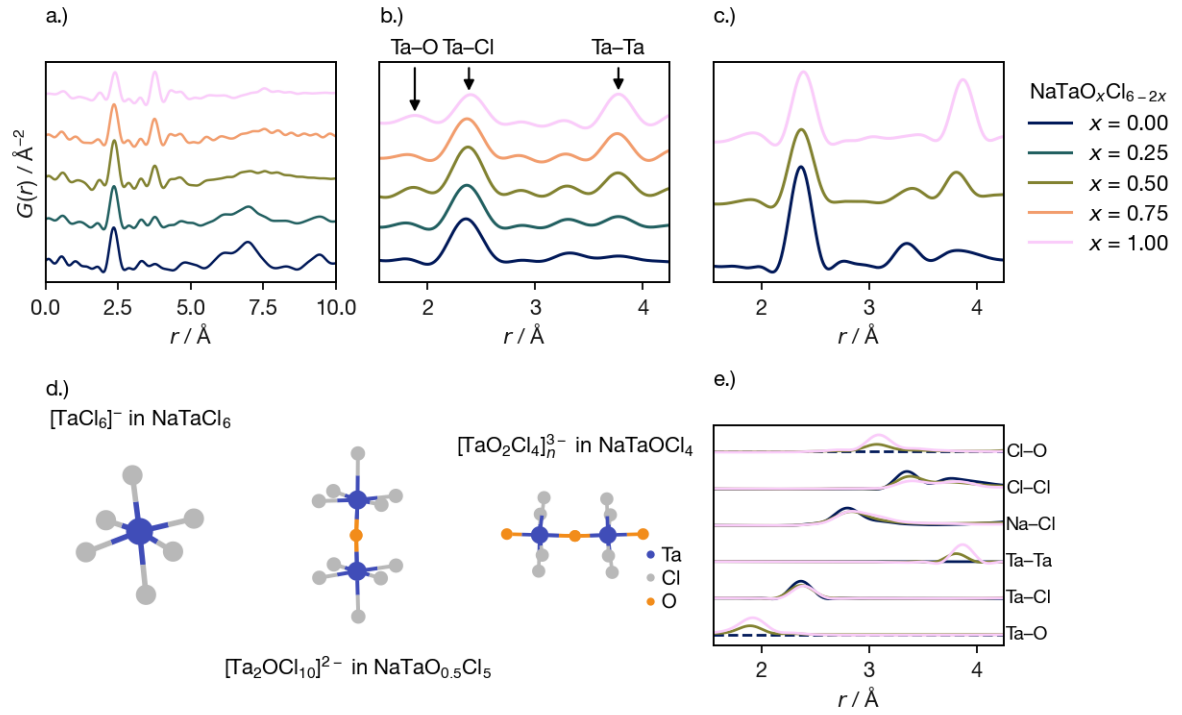

Figure 1 (a) Weighted experimental pair distribution function (PDFs) of $NaTaO_xCl_{6-2x}$ ranging from x = 0 to x = 1, vertically offset of 150 Å–2 for clarity. (b) Zoomed-in view of the experimental pair distribution functions for detailed comparison of interatomic distances. Key bond distances corresponding to the Ta–O, Ta–Cl, and Ta–Ta distances are highlighted. (c) Weighted simulated PDFs of DFT relaxed structures for $NaTaCl_6$, $NaTaO_{0.5}Cl_{5.0}$ and NaTaOCl4 illustrating the evolution of local environments with increasing oxygen content. (d) Local environments used for the comparison of pair distances with the experimental data, including the local structural motifs of $NaTaO_{0.5}Cl_{5.0}$ and $NaTaOCl_4$ derived from the DFT-simulations. (e) Changes in peak intensity for atom pairs across compositions x=0.00 x= 0.50, and x = 1.00, normalized to the highest peak in each plot across all simulated compositions.

The weighted pair distribution functions (PDF) of $NaTaO_xCl_{6-2x}$ (Figures 1a-b) confirm the progressive loss of long-range order across the series. At $x = 0.0$, the G(r) exhibits sharp peaks extending beyond ~7 Å, characteristic of crystalline $NaTaCl_6$.[9] Increasing oxygen content broadens these features, indicating a progressive loss of periodicity in agreement with the Bragg data and prior results as from Zhao *et al.*[12] or Huang *et al.*[14] Nevertheless, distinct short-range correlations persist even for $x \geq 0.5$, evidencing locally ordered motifs within an amorphous matrix.

To resolve the nature of the short-range features identified in the amorphous phases, simulated PDFs were constructed by Boltzmann-weighting the individual PDFs of DFT-relaxed structures generated through *ab initio* random structure searching (AIRSS) (Figure 1c) with compositions of x = 0, 0.5 and 1 ($NaTaCl_6$, $NaTaO_{0.5}Cl_5$, $NaTaOCl_4$, respectively)[15],[16]. To enable direct comparison with experiment, simulated PDFs were weighted with X-ray form factors.[17],[18] A closer look at the 1 – 5 Å region enables a more detailed comparison of local features across the compositional series (Figures 1b-e). For x = 0.0, a distinct peak near ~2.3 Å is observed, corresponding to Ta–Cl bonds; upon oxygen incorporation, new pair correlations emerge at ~1.9 Å and ~3.8 Å. The persistence of the Ta–Cl peak across the series suggests that the local Ta coordination environment remains largely octahedral, considering that changes in coordination would affect the bond length, even as long-range order diminishes. The ~1.9 Å peak is associated with Ta–O interactions, while the ~3.8 Å feature is assigned to Ta–Ta second shell coordination. For the x = 1 phase, the Ta–Ta peak increases in intensity compared to x = 0.5, indicating enhanced Ta–Ta clustering driven by the oxide-ion incorporation. Other features in the PDF, particularly those showing Q_{max}-dependent shifts in position and intensity, are attributed to Fourier truncation effects and should not be interpreted structurally (Figure S3).

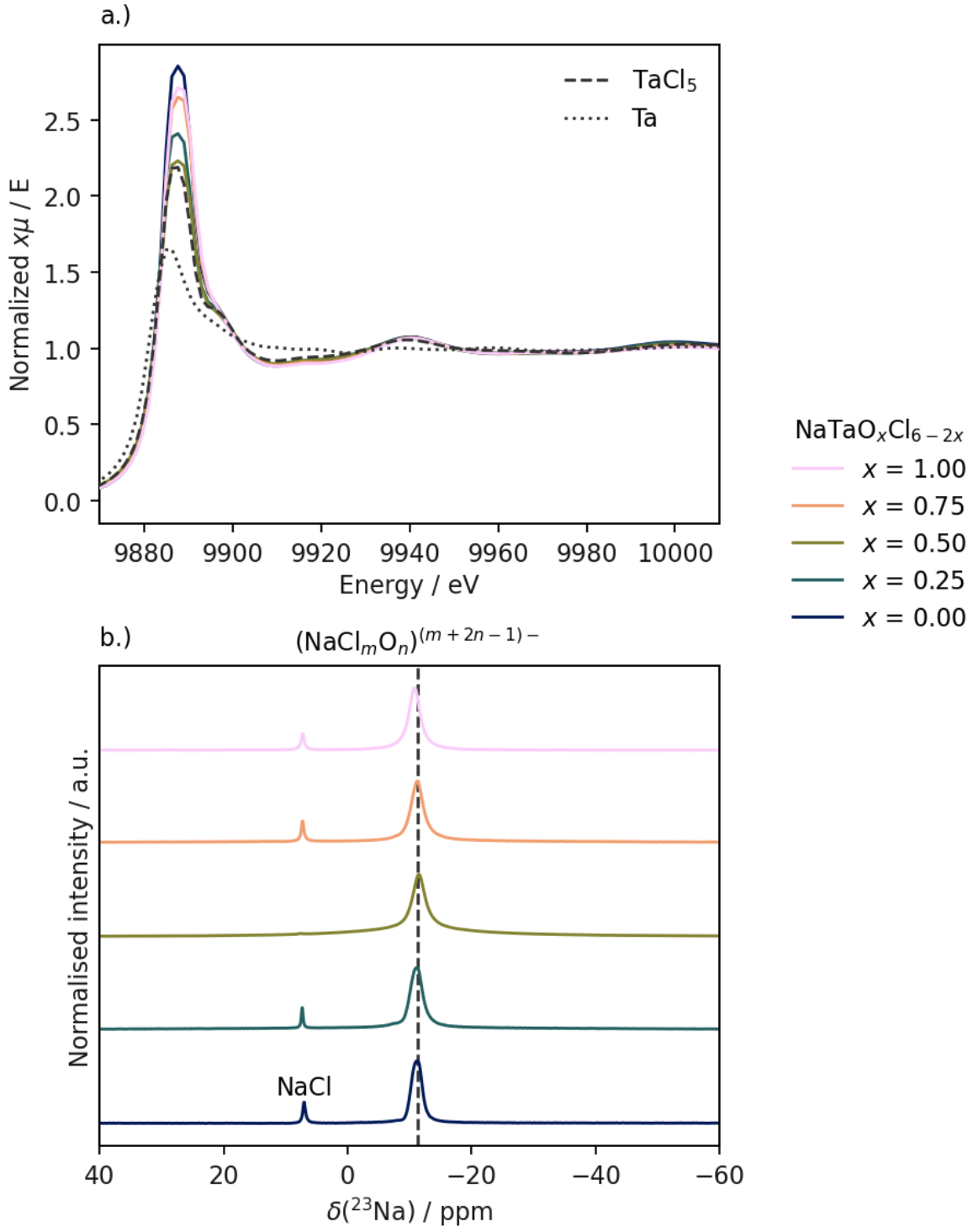

Figure 2. (a) Normalized XANES spectra for mixed-anion $NaTaO_xCl_{6-2x}$ oxychlorides samples at the Ta L3-edge showing all compositions coincide with the Ta^{5+} reference. (b) Stacked plot of the solid-state 23Na MAS NMR spectra of $NaTaO_xCl_{6-2x}$ ranging from x = 0 to x = 1 in steps of Δx = 0.25. The dashed line around -11.3 ppm is showing a shift of the Na-resonance in the substitution series.

To further examine the local structure and electronic environment, normalized Ta L_3-edge XANES spectra of $NaTaO_xCl_{6-2x}$ ($x = 0 - 1$) are collected alongside Ta metal and $TaCl_5$ references (Figures 2a, S4a). The absorption-edge positions and white-line maxima of all oxychloride compositions coincide with the Ta^{+5} reference and are shifted to higher energy relative to metallic Ta, confirming that tantalum remains in a d^0, +5 oxidation state across the series. The absence of any systematic edge shift indicates that oxide incorporation is accommodated structurally rather than through changes in Ta valence. EXAFS spectra reveal progressively damped oscillations with increasing oxygen content, consistent with the loss of structural coherence indicated by the PDF results (Figure S4b). As PDF, XANES and EXAFS probe more the anionic structural framework, the evolution of the local Na^+ coordination environments in the $NaTaO_xCl_{6-2x}$ series is probed using solid-state ^{23}Na MAS NMR spectroscopy.

As shown in Figure 2b and Figure S5a, the major ^{23}Na signals (narrow and broad) are centered between -4 to -12 ppm, with a minor signal around 7.3 ppm, corresponding to solid NaCl impurity. Integrated areas (Figure S5b, S6, Table S3) show this impurity to be very minor, in line with no NaCl Bragg reflections in the otherwise amorphous matrix. The experimentally observed narrow ^{23}Na signal around -11 ppm is characteristic of Na^+ in a disordered matrix containing Cl^- and O^{2-} anions.[19],[20],[21] In a recent study,[21] density functional theory reveals that the negative chemical shift of ^{23}Na in $NaCl_mO_n$-type ($1 \leq m \leq 3$, $3 \leq n \leq 6$) local environments can vary from -3.8 ppm to -12.6 ppm based on the coordination number (six or eight), geometry, and the Cl^-/O^{2-} ratio. $NaCl_3O_3$, $NaCl_4O_2$ and $NaCl_6O_2$ environments show ^{23}Na chemical shifts of -10.3, -11.0 and -12.6 ppm, respectively. Thus, the observed trend in the changing ^{23}Na chemical shift (Figure S5a) for the sharp ^{23}Na resonance possibly results from the coexistence of different $NaCl_mO_n$-type local Na^+ coordination environments in varying amount based on the oxygen content, whereas the broad ^{23}Na resonance arises from the disordered nature of the sample with a significant fraction of Na^+ with different localized mobilities in anisotropic coordination environments.

Local structural preference. To rationalize the observations seen in PDF, XAS, and NMR analyses and to probe the range of atomic arrangements consistent with them, we analyzed the full ensemble of configurations generated through AIRSS for $x = 0.5$ and $x = 1$. The resulting structural ensemble was deemed physically representative based the comparison of densities

with experiment (see Supplementary Note 6, Figure S7). Each structure was characterized by the local chemical environments around Ta encoded using Smooth Overlap of Atomic Positions (SOAP) descriptors[22]. The resulting high-dimensional SOAP power spectra were projected into a two-dimensional space using Pairwise Controlled Manifold Approximation Projection (PaCMAP), a manifold-learning technique that preserves both global and local structural relationships.[23] This approach, previously applied to complex crystal-structure prediction datasets, enables coarse visualization of the configurational and energetic landscape (Figure S7), identifying structural motifs present in low energy structures. The PaCMAP embeddings reveal distinct clusters corresponding to characteristic Ta–O and Ta–Cl coordination environments, providing an atomistic picture of how local structure changes across the series (Figure 3).

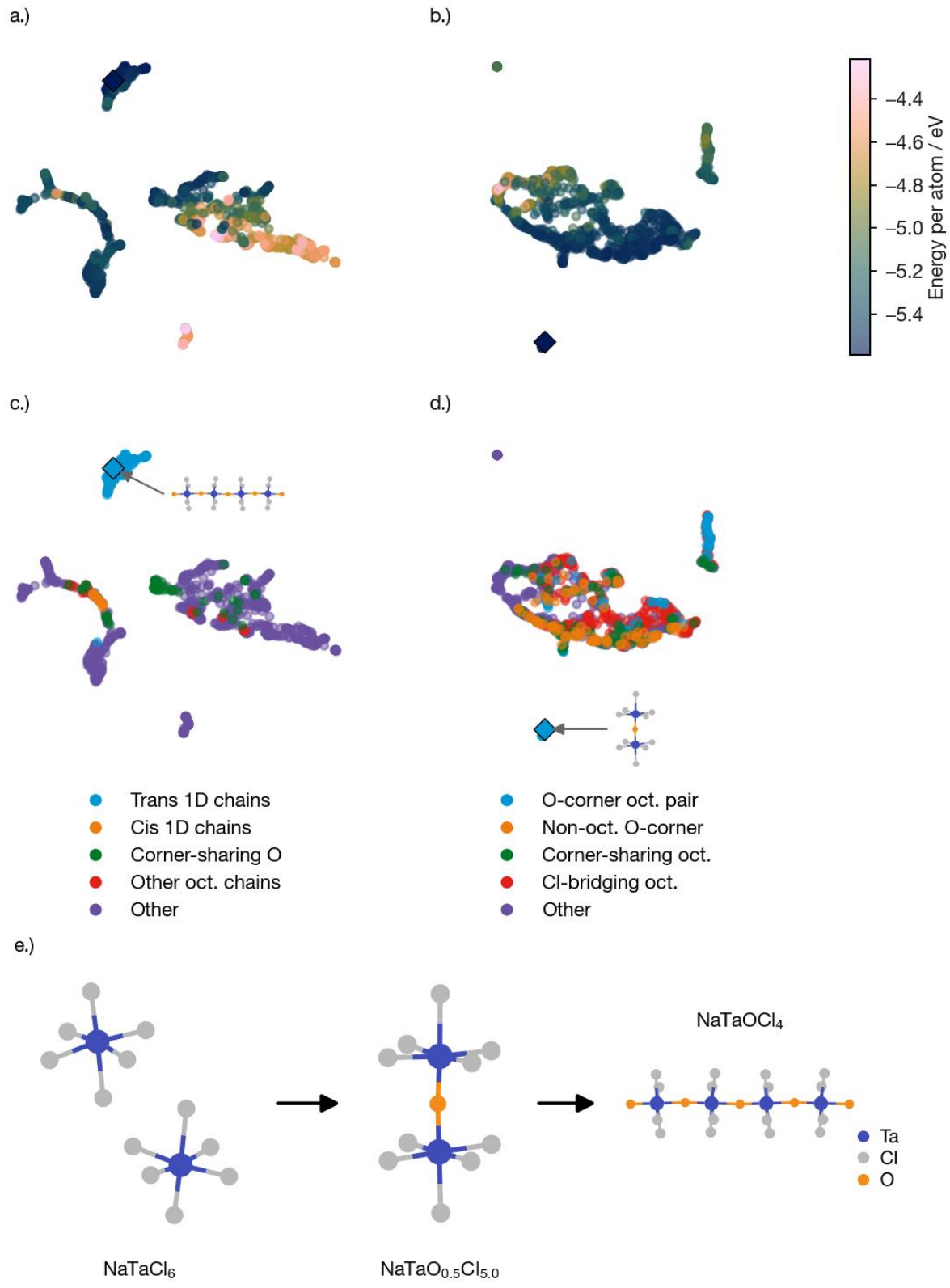

Figure 3. Two-dimensional representation of the SOAP vectors describing the average local Ta environments for each structure in the AIRSS ensemble of (a) $NaTaOCl_4$ and (b) $NaTaO_{0.5}Cl_{5.0}$. Dimensionality reduction was performed using PaCMAP, with the color scale indicating the energy per atom of each structure. Panels (c) and (d) show the same embeddings, colored

instead by categorical Ta environments. In all panels (a–d), the lowest-energy structure is marked with a diamond. (e) Schematic illustration of the proposed structural evolution across the $NaTaO_xCl_{6-2x}$ series (x = 0.0, 0.5, 1.0), focusing on Ta coordination environments (Ta: blue, O: orange, Cl: grey). Oxygen substitution promotes the formation of corner-sharing Ta–O–Cl polyhedra. At intermediate composition (x = 0.5), local preferences favor $[Ta_2OCl_{10}]^{2-}$ dimers, which evolve into trans-$[TaO_2Cl_4]^{3-}$ chains at higher oxygen content (x = 1.0).

In crystalline $NaTaCl_6$ ($x = 0$), each Ta^{5+} center forms an isolated $[TaCl_6]^-$ octahedron, forming a fully disconnected, zero-dimensional framework. The addition of oxygen induces octahedra connectivity. In $NaTaOCl_4$ ($x = 1$), the lowest-energy configurations exhibit one-dimensional chains of trans-$[TaO_2Cl_4]^{3-}$ octahedra, in which the two O^{2-} ligands occupy opposite apical sites and bridge adjacent Ta^{5+} centers (Figures 3c, 3e). This is consistent with the increasing intensity of Ta–O and Ta–Ta correlations seen in the PDFs as oxygen content increases. The preference for the trans configuration mirrors that reported for $LiNbOCl_4$,[19],[24] and arises because the formation of these one-dimensional trans chains simultaneously maximizes Ta–O bonding and minimizes electrostatic repulsion between neighboring octahedra (Supplementary Note 7, Figure S8). However, the small energetic separation between these ideal and alternative motifs (such as other corner-sharing Ta–O–Ta connections, octahedral or otherwise) indicates that, in real systems, the ideal trans chains are likely to be highly defective or locally disrupted by distortions and non-octahedral units, which may explain the relative lack of crystallinity in the Na-oxyhalides as compared to Li-analogues, despite similar bonding preferences.

Extending this analysis to $x = 0.5$ shows that the same local connectivity rules apply, but the reduced oxygen content weakens the structural coherence imposed by chain formation. At this composition, the calculations reveal an energetic preference for pairs of $[TaOCl_5]^{2-}$ octahedra connected through a corner-sharing O^{2-} ion (Figures 3d, 3e). The zero-dimensional nature of these dimeric units relaxes the configurational constraints associated with the extended one-dimensional chains preferred at $x = 1$, giving rise to a highly degenerate and locally disordered ensemble. Taken together, these results show that oxygen incorporation first destabilizes the halide lattice, generating a disordered intermediate regime at moderate substitution, but ultimately restores connectivity through the emergence of Ta–O–Ta linkages that yield a preference for a disordered yet structurally coherent network evidenced by the increasing Ta–Ta peak intensity as x increases in the PDF data (c.f. Figure 1e).

Ionic transport as a function of framework coherence. AC impedance spectroscopy reveals a strong composition-dependent evolution in ionic conductivity across the $NaTaO_xCl_{6-2x}$ series (Figure 4a, Supplementary Note 8). To ensure reproducibility and accurately determine the conductivity maximum, every second composition was measured in triplicate. The conductivity sharply increases with x by nearly two orders of magnitude relative to $NaTaCl_6$ (5.2×10^{-2} mS·cm^{-1}), reaching a maximum of ≈ 4 mS·cm^{-1} at $x = 0.5$ and remains high for $0.5 < x < 1.0$. Ensemble analysis indicates that the configurations containing $TaOCl_5$-like units linked through bridging oxides are energetically favored at this composition, giving rise to local connectivity without long-range order. This structural heterogeneity creates a broad spectrum of Na^+ environments and diffusion pathways that collectively facilitate transport. At $x = 1.0$, oxygen substitution promotes greater Ta–O–Ta coherence through the increased population of trans-TaO_2Cl_4-like chain motifs, which correlates with a slight reduction in ionic mobility. These results indicate that locally connected but structurally disordered environments are most conducive to Na^+ transport, whereas increased framework coherence begins to suppress ionic motion by reducing configurational diversity.

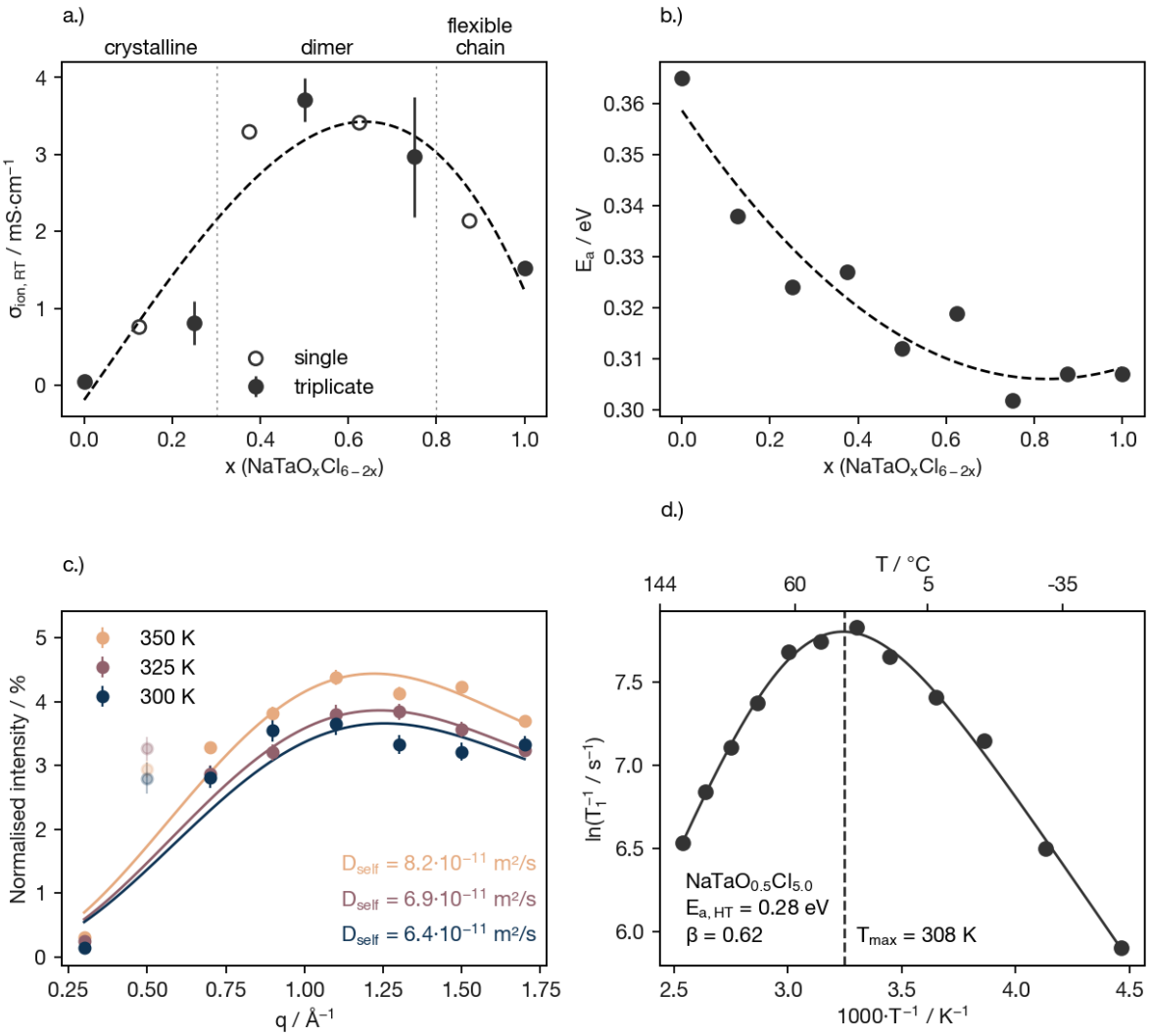

Figure 4. (a) Room-temperature ionic conductivities ($\sigma_{ion,RT}$) of $NaTaO_xCl_{6-2x}$ as a function of oxygen content (x). The graph is divided into three composition regimes, reflecting distinct structural motifs, revealing a trend in conductivity correlated with increasing oxygen content. (b) Activation energies (E_a)) showing a downward trend as chloride is progressively replaced by oxide anions. (c) Application of the Chudley-Elliott model to the QENS data of $NaTaO_{0.5}Cl_{5.0}$, yielding high the self-diffusion coefficients (D_{self}) for Na^+. Transparent data points denote outliers excluded from the fit. (d) Arrhenius plot of the ^{23}Na NMR T_1-relaxation rate of $NaTaO_{0.5}Cl_{5.0}$. The solid line represents fit according to the modified Bloembergen, Purcell, and Pound (BPP) model. Position of the T_{max} is indicated by the vertical dashed line.

Activation energies decrease from ≈ 0.37 eV for $NaTaCl_6$ to ≈ 0.31 eV for oxygen-substituted compositions (Figure 4b), stabilizing for $x \geq 0.5$. This flattening of the energy landscape suggests that once a critical amorphization level is reached, similar Na^+ environments dominate

continuous and efficient ion transport. The composition x = 0.5 emerges as particularly favorable, combining the highest ionic conductivity with the most structurally heterogenous motif distribution among the amorphous phases. To gain more microscopic insight into the Na^+ diffusion of this composition, quasielastic neutron scattering (QENS) is performed (Supplementary Note 9). The energy spectra (Figure S12a) show increasing quasielastic broadening with rising temperature, indicative of thermally activated Na^+ dynamics. The full width at half maximum (Γ) of the quasielastic component increases with momentum transfer q and reaches a plateau at higher q-values (Figure 4c), consistent with localized jump diffusion behavior. Fitting the $\Gamma(q)$ dependence using the Chudley-Elliott model yields jump lengths and mean residence times (Table S5) which were used to calculate Na^+ self-diffusion coefficients (D_{self}) ranging from $6.6 \cdot 10^{-11}$ to $8.2 \cdot 10^{-11}$ $m^2 \cdot s^{-1}$ increasing with temperature. These values are characteristic of fast-ion conductors and align well with estimates derived from macroscopic ionic conductivity measurements (Figure S13), confirming that the high Na^+ transport arises from short-range, thermally activated diffusion events in the amorphous matrix. Based on this comparison, the fraction of mobile Na^+ ions is estimated to be approximately 1 – 5%, increasing with temperature (Figure S14). This fraction reflects the portion of Na^+ ions undergoing dynamic motion on the QENS timescale (ps to ns). The Na^+ dynamics is further probed using ^{23}Na NMR spin-lattice relaxometry (SLR), being sensitive to Na^+ motions (Figure 4d, S15 a-c). Analyzing the SLR data with a modified BPP model provides two different activation energies – $E_{a,HT}$ (from the high-temperature flank) and $E_{a,LT}$ (from the low-temperature flank) that corresponds to the long-range ($\omega_0\tau_c << 1$) and short-range ($\omega_0\tau_c >> 1$) Na^+ diffusion, respectively.[25] The difference between the two activation energies lead to an asymmetric appearance of the rate curve, which is quantified using the asymmetry parameter β ($0 < \beta \leq 1$). For three-dimensional uncorrelated motion, β equals to unity, leading to a symmetric rate curve. However, for ionic motions in solid electrolytes, the value of β is generally less than 1, due to the correlated motions in these solid electrolytes as a result of structural complexity coming from Coulombic interactions, local disorders *etc*.[26],[27] Fitting the data using modified BPP model revealed an increase in $E_{a,HT}$ from ~ 0.27 eV for $x \leq 0.5$ to ~ 0.32 eV for $x > 0.5$, whereas $E_{a,LT}$ showed a maximum of 0.17 eV for x = 0.5 (Figure S15d). The asymmetry parameter β is determined to be the highest (= 0.62) for x = 0.5 (Figure S15e), dropping to ~ 0.36 for $x > 0.5$. Taken together, the localized Na^+ motion is found to be strongly affected by the presence of different local motifs, where the x = 0.5 sample showed the least correlated ionic motion (highest β) due to the high structural heterogeneity offered by the $TaOCl_5$-like units linked through bridging oxide anions. The emergence of trans-TaO_2Cl_4-like

chain motifs at higher oxygen content significantly reduces the localized Na^+ jump frequencies via reducing the configurational diversity, which results in a drastic high-temperature shift of the T_{max} by 70 K going from x = 0.5 to x = 1.0 (Figure S15e). Furthermore, the self-diffusion coefficient from NMR (D_{NMR}) for x = 0.25, 0.5 and 0.75 is calculated to be in the order of 10^{-12} $m^2 \cdot s^{-1}$ at 300 K, using the random walk model and the jump distance obtained from QENS analysis (Supplementary Note 10, Table S5). The difference between D_{NMR} and $D_{Nernst\text{-}Einstein}$ (Figure 4c) possibly arise from the fact that D_{NMR} likely is affected by large number of unsuccessful jump processes, that are not present in $D_{Nernst\text{-}Einstein}$, as the later probes successful longer-range ionic jumps only.[28],[29]

Application of amorphous oxyhalides in sodium solid-state batteries. To evaluate the electrochemical performance of $NaTaO_xCl_{6-2x}$ catholytes, solid-state battery cells were assembled using $Na_{2/3}Ni_{1/3}Fe_{1/3}Mn_{1/3}O_2$ (NFM) as the cathode active material, $Na_2(B_{10}H_{10})_{0.5}(B_{12}H_{12})_{0.5}$ as separator and $Na_{2.25}Sn$ as anode material. Figure 5a displays a representative voltage–capacity curve for x = 0.5, demonstrating reversible charge-discharge behavior between 2.2 and 3.4 V, along with the corresponding capacity evolution over 350 cycles (Figure 5b). The electrochemical stability of $NaTaOCl_4$ has previously been evaluated by linear sweep voltammetry, demonstrating stability within the applied voltage window.[13] Accordingly, a cycling window of 2.2–3.4 V was selected to avoid decomposition of both the oxyhalide electrolyte and the Na-hydroborate separator. The initial discharge capacity of 75 $mAhg^{-1}$ gradually decreases to 38 $mAhg^{-1}$ after 350 cycles, equivalent to a capacity retention exceeding 50%, likely due to interfacial processes (e.g. CEI formation) or local contact loss associated with volume changes of the NFM.[12],[30] Notably, the rate of capacity decay diminishes with increasing cycling number, indicating a progressive stabilization of the electrochemical interfaces. Analogous data for other compositions are provided in Supplementary Note 11 (Figure S16-17). Rate performance trends (Figure 5c) mirror the ionic conductivities of the corresponding electrolytes. $NaTaCl_6$ exhibits the lowest rate capability, whereas oxygen-substituted compositions with higher conductivities deliver improved performance at high-rates. Plotting discharge capacity against room-temperature ionic conductivity (Figure 5d) reveals a general correlation, though deviations occur at the highest conductivities, suggesting that factors beyond bulk ion transport, such as particle size distribution and interparticle connectivity, affect rate behavior.[31] Further insight into the degradation process was obtained from impedance measurements collected during the first 20 cycles (Figure S18). These spectra reveal a gradual increase in impedance for all cells during

cycling. While the initial impedance follows the trend of the solid electrolyte ionic conductivities, the rate of increase growth varies the compositions. In particular, the impedance of the $NaTaO_{0.5}Cl_{5.0}$-based cell increases more rapidly than those of cells with x = 0.25, 0.75 and 1.00, indicating a faster degradation process. Indeed, scanning electron microscopy and a corresponding particle size analyses (Supplementary Note 12, Figures S19-20) shows that $NaTaO_{0.5}Cl_{5.0}$ possesses the largest particle size, which may impede the homogeneous percolation of ionic and electronic transport networks even after processing into composites.[32] Clearly, while bulk transport properties can be optimized in these oxyhalide solid electrolytes through oxygen incorporation, for cell application the microstructure will require some further optimization in future work.

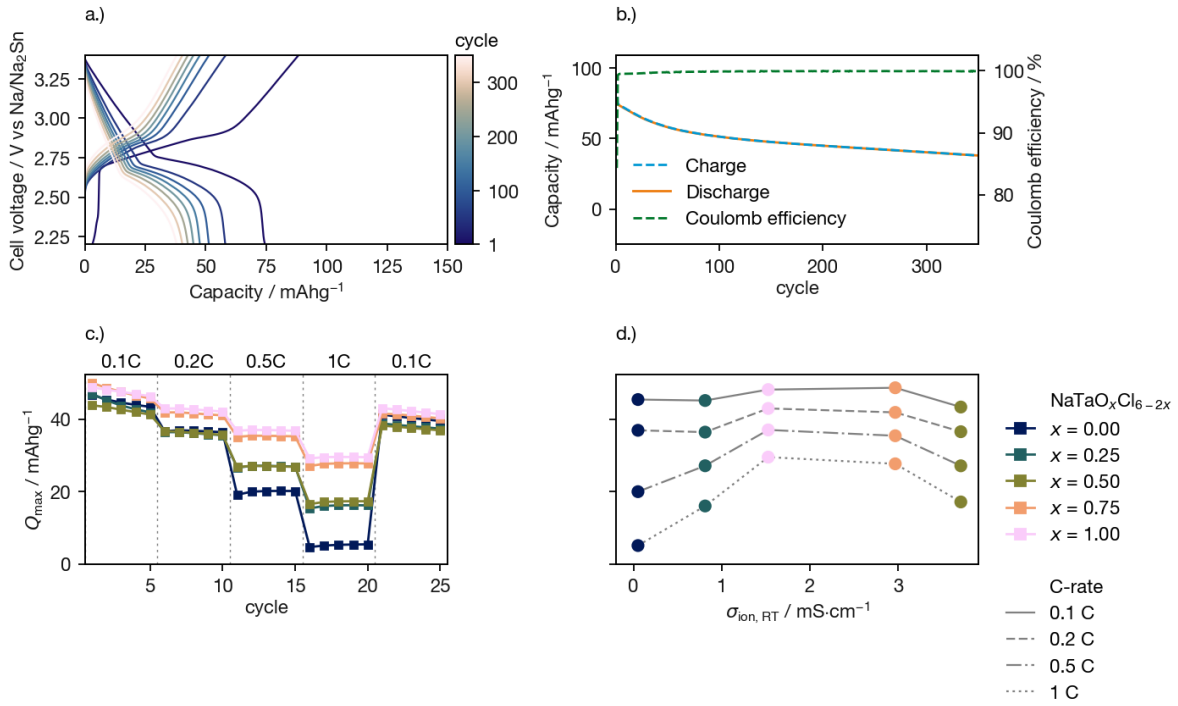

Figure 5. (a) Representative charge–discharge curves for every 50th cycle of the $Na_{2.25}Sn$ | $Na_2(B_{10}H_{10})_{0.5}(B_{12}H_{12})_{0.5}$ | NFM:$NaTaO_{0.5}Cl_{5.0}$:CNF solid state batteries (x = 0.5) at room temperature, demonstrating reversible cycling behavior. (b) Representative long-term cycling performance of the same sodium solid state batteries (x = 0.5) at room temperature, showing an initial capacity decay followed by stabilized cycling. (c) Rate performance of full cells with different $NaTaO_xCl_{6-2x}$ catholytes, measured between 2.2 and 3.4 V. (d) Correlation between the maximum discharge capacity and room-temperature ionic conductivity of the corresponding solid electrolytes.

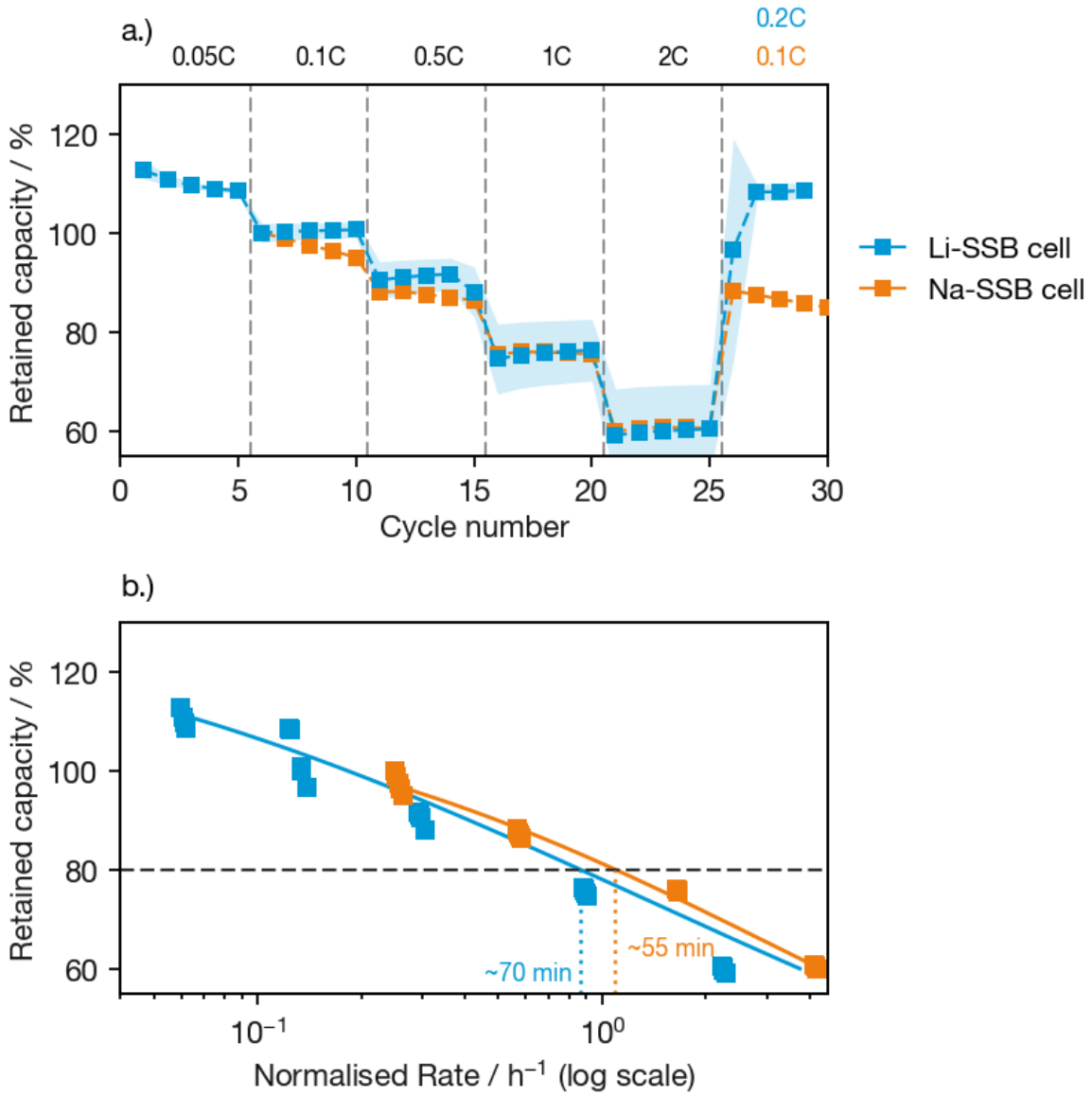

Figure 6. (a) Comparison of the retained discharge capacity (%) as a function of cycle number for a lithium solid-state battery (LSSB)- data from ref. 33 - and the sodium solid-state battery (NSSB) of this work using $NaTaO_{0.75}Cl_{4.5}$ as solid electrolyte. (b) Retained discharge capacity (%) as a function of inverse discharge time (h^{-1}), illustrating a slightly faster capacity decay of the sodium system.

To benchmark the performance of the $NaTaO_xCl_{6-2x}$ catholytes, the electrochemical behavior of the sodium solid-state battery (x = 0.75), which exhibits the highest capacities in the rate tests and high ionic conductivity, was compared to that of a lithium solid-state battery (LSSB) reported by Schlautmann *et al.* (Figure 6) with optimized particle sizes of a Li_6PS_5Cl solid electrolyte.[33] As shown in Figure 6a, the sodium-based system exhibits stable cycling with

moderate capacity fading over repeated cycles, following a trend comparable to that of the lithium-based reference. The discharge capacities are normalized to the first cycle at 0.1C to enable a direct comparison of capacity retention. Although the absolute capacity of the sodium active material is lower, the overall evolution of rate performance is similar. Comparing the retained discharge capacity as a function of inverse discharge time (Figure 6b) reveals a systematic decrease in capacity with increasing rate for both systems.[34],[35] Notably, the sodium solid-state battery shows a rate-dependent behavior closely resembling that of the lithium system, despite the intrinsically lower ionic conductivity and larger ionic radius of Na^+ compared to Li^+. This indicates that the oxyhalide electrolyte enables efficient Na^+ transport even under kinetically demanding conditions. Overall, this comparison demonstrates that the sodium system approaches the electrochemical performance of established lithium solid-state batteries in terms of rate capability. These findings highlight the potential of mixed-anion oxyhalide electrolytes as a promising materials platform for sodium solid-state batteries.

Na^+ transport from ab initio molecular dynamics. Experimental results show that compositions with intermediate oxygen content exhibit the highest bulk ionic conductivity. To test whether this is consistent with atomistic transport behavior, ab initio molecular dynamics (AIMD) simulations are performed on representative local configurations of $NaTaO_xCl_{6-2x}$ at x = 1 (112 atoms) and x = 0.5 (120 atoms), capturing the oxygen-rich and intermediate compositions that favor locally connected (chain-like) and less-connected (dimer-like) Ta environments, respectively. Starting configurations are drawn from the AIRSS-generated structural ensemble, with both the lowest-energy structures and selected thermally accessible higher-energy configurations included to probe the effect of local structural variation on Na^+ dynamics.

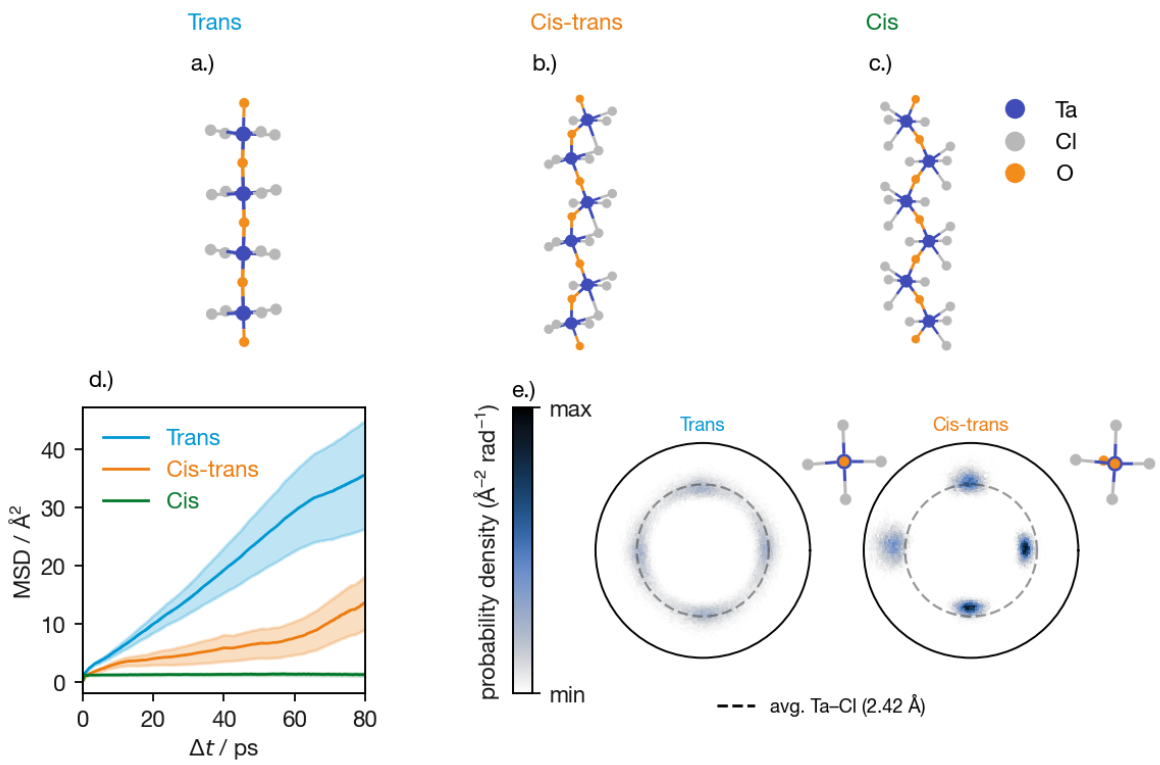

Figure 7. Representative motifs of the $NaTaOCl_4$ composition. (a) exclusively trans-$[TaO_2Cl_4]^{3-}$ chains, (b) alternating cis-trans octahedra, (c) cis-only chains. (d) Na^+ mean-squared displacements from AIMD simulations for each motif; the trans structure shows markedly enhanced Na^+ mobility relative to the cis and cis-trans arrangements. (e) Probability density maps of equatorial ligand orientations about the Ta–O–Ta axis for trans octahedra in the cis-trans and trans only structures; the dashed circle marks the average Ta–Cl bond length (2.42 Å). The trans octahedra exhibit a broad, near-uniform angular distribution, indicating large-amplitude rotational freedom, whereas the cis-trans octahedra show sharply localized density, reflecting constrained ligand motion.

For $x = 1$ ($NaTaOCl_4$), simulations of three representative local configurations — pure trans chains, cis-only chains, and alternating cis-trans arrangements (Figures 7a–c) — show that Na^+ exhibits the largest mean-squared displacement in the trans structure (Figure 7d). The trans-only framework displays substantial collective flexibility, characterized by large-amplitude rotations of the equatorial Cl_4 plane (Figure 7e; full framework trajectories and additional polar maps are provided in Supplementary Note 13, Figures S21–23). In contrast, the trans octahedra in the cis-trans structure exhibit restricted motion due to edge-sharing between octahedra, which mechanically locks the framework and suppresses rotational freedom.[36] Although the

cis-only structure is formally corner-sharing, the fact that both bridging oxygens lie along the same edge creates an effectively edge-sharing arrangement, similarly constraining rotation. The enhanced Na^+ mobility in the trans-only chains is consistent with a "soft cradle" mechanism analogous to that proposed for $LiNbOCl_4$,[19],[37] in which cooperative rotational fluctuations of the framework octahedra flatten the potential energy surface for Na^+ transport and facilitate cation hopping.

These results establish a correlation between framework flexibility and Na^+ diffusivity at x = 1. Importantly, polyhedral connectivity and rotational freedom are not independent variables — the mode of connectivity governs the degree of rotational freedom available to the framework, such that the MSD differences between motifs reflect a single coupled structural effect. This also has a broader implication: the fast ion transport observed experimentally need not be a direct consequence of amorphicity, but rather of the flexible local motifs that promote Na^+ mobility.

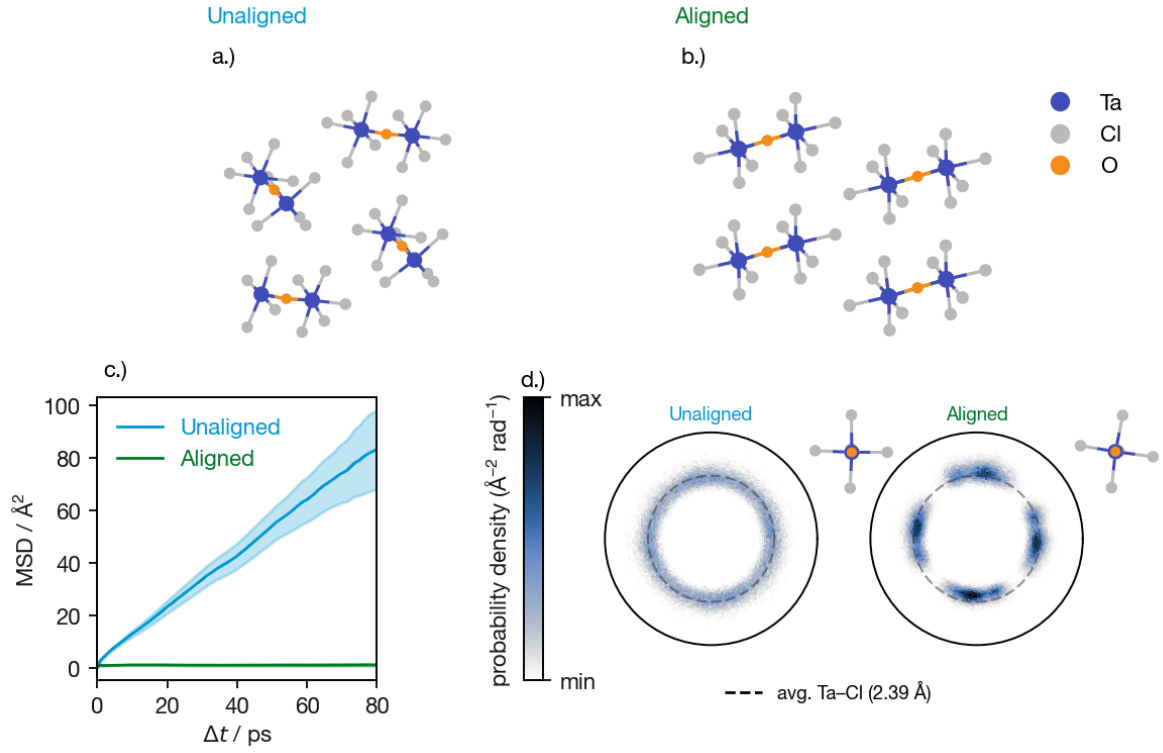

Figure 8. Representative motifs of the x = 0.5 composition. (a) Unaligned configuration (b) Aligned configuration, in which all Ta–O–Ta linkages adopt a parallel orientation. (c) Na^+ mean-squared displacements from AIMD simulations for each motif; the unaligned structure shows markedly enhanced Na^+ mobility. (d) Probability density maps of equatorial Cl ligand

orientations about the Ta–O axis; the dashed circle marks the average Ta–Cl bond length (2.39 Å). The unaligned structure exhibits a broad, near-uniform angular distribution indicative of large-amplitude rotational freedom, while the aligned structure shows sharply localized density, reflecting constrained ligand motion.

For $x = 0.5$ ($NaTaO_{0.5}Cl_5$), AIMD simulations were performed on two representative motifs (Figure 8a, 8b) to probe how dimer orientation influences Na^+ mobility. The lowest-energy configuration, comprising ordered $[Ta_2OCl_{10}]^{2-}$ dimers with all Ta–O–Ta linkages in a parallel orientation (Figure 8b), show minimal Na^+ mobility (Figure 8c). This high degree of orientational coherence is unlikely to be representative of the experimentally observed amorphous phase. To investigate the effect of relative dimer orientation, an additional configuration from the AIRSS ensemble (22.4 meV $atom^{-1}$ above the ground state) was selected for simulation (Figure 8a, Supplementary Note 14, Figure S24). In this structure Na^+ diffusion is markedly enhanced and correlates with increased rotational freedom of the equatorial Cl_4 plane in the $[TaOCl_5]^{2-}$ octahedra (Figure 8c, 8d) — consistent with the same flexibility–mobility relationship identified at $x = 1$.

The computed diffusion coefficients across all five structures span nearly two orders of magnitude — from $1.3 \pm 1.0 \times 10^{-11}$ m^2 s^{-1} (Aligned dimers) and $1.5 \pm 0.8 \times 10^{-11}$ m^2 s^{-1} (Cis chains) up to $4.8 \pm 1.1 \times 10^{-10}$ m^2 s^{-1} (Trans chains) and $1.1 \pm 0.2 \times 10^{-9}$ m^2 s^{-1} (Unaligned dimers) — and correlate strongly with the rotational standard deviation *s* of equatorial ligands about the Ta–O(–Ta) axis (Figure 9), reinforcing that rotational flexibility is a key determinant of Na^+ mobility in these systems, consistent with observations in lithium analogues[19]. By contrast, no systematic trend was found between diffusivity and fluctuations in either the Ta–O–Ta bridging angle or the Ta–O/Ta–Cl bond lengths (Figure S25), indicating that bond-geometry distortions along the chain backbone are not the primary determinant of Na^+ mobility. The simulated transport results are further discussed in the context of free volume for Na^+ diffusion in Supplementary Note 16 and Figures S26–28; although free volume metrics capture the broad trend that more open frameworks facilitate diffusion, they fail to reproduce Na^+ mobility trends at the level of specific local configurations, further supporting that rotational flexibility of the equatorial ligands is the primary determinant of Na^+ transport.

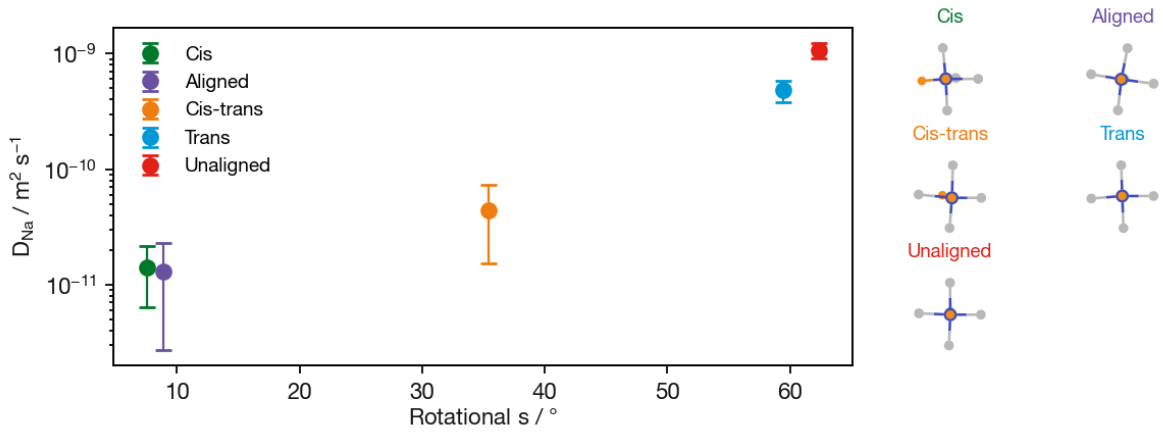

Figure 9. Na^+ diffusion coefficient D_{Na} versus rotational amplitude s of the equatorial ligands for each molecular dynamics simulation performed. s is the standard deviation of the azimuthal angle of each equatorial ligand in the plane perpendicular to the Ta–O(–Ta) axis in each polyhedron with each ligand's time-averaged position subtracted to isolate thermal motion. D_{Na} is obtained from a Bayesian fit to the Na^+ mean-square displacement over 80 ps; error bars are posterior standard deviations.

CONCLUSION

In this work, the mixed-anion series $NaTaO_xCl_{6-2x}$ ($0 \leq x \leq 1$) was systematically investigated to unravel how oxygen incorporation tunes structure and ionic transport in amorphous sodium tantalum oxyhalides. By integrating experimental and computational methods, we demonstrate that while long-range order is lost upon oxygen substitution, distinct short-range structural motifs persist and dominate the transport behavior. Oxygen incorporation induces amorphization because oxygen atoms preferentially coordinate with multiple Ta centers, maximizing local electroneutrality and disrupting long-range order. At intermediate oxygen content ($x = 0.5$), the network is composed primarily of oxygen-bridged $[Ta_2OCl_{10}]^{2-}$ dimers, whose random orientations and flexible linkages create a dynamically soft framework with a flat energy landscape for Na^+ migration. This structural configuration yields the highest room-temperature ionic conductivity of ≈ 4 mS·cm^{-1} and Na^+ self-diffusion coefficients up to 8.2×10^{-11} m^2·s^{-1}. In contrast, the more ordered trans-$[TaO_2Cl_4]^{3-}$ chains that emerge at $x = 1$ introduce directional coherence and reduced flexibility, constraining Na^+ mobility.

These findings establish that ionic transport in amorphous oxyhalides is not governed by long-range periodicity, but local flexibility and orientational disorder within the Ta–O–Cl framework plays a primary role. The interplay between small, disordered structural units and extended but flexible chain motifs define the optimal balance between stability and mobility. This insight provides a fundamental design principle for developing next-generation superionic conductors, where controlled local disorder and mixed-anion coordination can be leveraged to achieve fast ion transport in amorphous and glass-ceramic solid electrolytes for sodium-based energy storage.

Methods

Synthesis. Sodium metal oxyhalides were synthesized via a mechanochemical route using ball milling under inert argon atmosphere conditions as recently described.[12] The stoichiometry was controlled by varying the ratio of precursors according to the following reaction:

$$x\ \mathrm{NaOH} + (1\text{-}x)\ \mathrm{NaCl} + \mathrm{TaCl_5} \rightarrow \mathrm{NaTaO_xCl_{6-2x}} + x\ \mathrm{HCl\ (g)}$$

Here, x with a targeted range of $0 \leq x \leq 1$ with steps of 0.125 represents the fractional amount of oxygen incorporated into the final product. Stoichiometric amounts of anhydrous NaOH (Sigma-Aldrich, 99.99%), anhydrous NaCl (Sigma-Aldrich, 99.995%), and anhydrous $TaCl_5$ (Alfa Aesar, 99.995%) were combined with zirconia (ZrO_2) milling media (5 mm diameter) in 80 ml ball milling cups, maintaining a mass ratio of 1:30 between the expected product and the milling media. As a premixing step, a planetary ball mill (Fritsch Pulverisette 7) was operated for 10 minutes each at 150 rpm and 300 rpm, respectively. The main mechanochemical reaction was then carried out under reverse milling mode at 500 rpm for 120 cycles, with each cycle consisting of 15 minutes of milling followed by a 5-minute cooling interval.

X-ray Diffraction (XRD). X-ray diffraction data were collected using a Stoe STADI P diffractometer equipped with Mo $K\alpha_1$ radiation ($\lambda = 0.70930$ Å) and a Ge (111) monochromator in Debye-Scherrer geometry. Diffraction patterns were recorded using a Dectris Mythen2 2K detector. The samples were sealed in borosilicate glass capillaries (0.5 mm diameter) to prevent air exposure during measurement and scanned over a 2θ range of 5° to 45° at a scanning rate of 0.67° per minute with a detector threshold of 8.74 keV. To quantify the amorphous content, lanthanum hexaboride (LaB_6, Alfa Aesar, 99.5%) was mixed with the samples as an internal standard. The known mass ratio of LaB_6 to sample, combined with phase analysis performed using TOPAS Academic V7, enabled determination of the amorphous fraction in the samples.[38]

Pair Distribution Function (PDF). Total scattering data were collected using a Stoe STADI P diffractometer with Ag $K\alpha_1$ radiation ($\lambda = 0.55941$ Å) and a Ge (111) monochromator in Debye-Scherrer geometry. The instrument was equipped with four Dectris MYTHEN2 4K detectors, as described by Thomae et al.[39] Samples were sealed in borosilicate glass capillaries and measured over a Q-range of 0.8 to 20.5 $Å^{-1}$ for a total acquisition time of 24 hours. Data reduction was performed using PDFgetX3 software, which applies Fourier transformation to convert the total scattering data into the pair distribution function.[40] For analysis, a Q-range cutoff (Q_{max}) of 15 $Å^{-1}$ was selected, with additional cutoffs at 13 $Å^{-1}$ and 18 $Å^{-1}$ applied for comparison.

X−Ray Spectroscopy (XAS): Extended X−ray absorption fine structure (EXAFS) experiments were carried out at the materials science beamline 10 at the DELTA storage ring (TU Dortmund/Germany) operating with 1.5 GeV electrons and a stored current of 100−130 mA (Range: 4−14 keV). A Si (111) channel-cut monochromator was employed, and the intensity of the incident beam on the sample was measured using a nitrogen−gas filled ionization chamber, while the X−ray fluorescence from the sample was collected using a large−area PIPS® photodiode (Passivated Implanted Planar Silicon).[41] The energy range measured covered the X−ray absorption L_3 edge of Ta (9881.1 eV). Initial data processing of the XANES region was performed via the ATHENA Software package.[42] Pre-edge range and spline range were determined from the automated data processing, while the edge step E_0 was obtained from the inversion point of the first major peak of the first derivative of μ(E). All data sets were plotted using normalization order 3. Because $NaTaO_xCl_{6-2x}$ oxychlorides are highly air- and moisture-sensitive, all handling was performed in an argon-filled glovebox (O_2 and H_2O < 0.1 ppm). Powdered samples were loaded into custom rectangular stainless-steel templates (5 × 3 cm^2) with a central aperture. The powders were carefully pressed into the aperture and hermetically sealed between two Kapton® adhesive foils, yielding mechanically stable and X-ray transparent pellets. This procedure ensured that no part of the sample was exposed to ambient atmosphere during mounting. After preparation, each sealed sample was immediately transferred into airtight 50 mL polypropylene Falcon® tubes, backfilled with argon, and stored until measurement. Samples remained fully isolated from air and moisture throughout all stages of storage, transport, and analysis.

Nuclear Magnetic Resonance Spectroscopy (NMR). Magic-angle spinning (MAS) NMR spectra of ^{23}Na (Larmor frequency ω_L = 132.36 MHz) were recorded on a Bruker NEO 500 spectrometer equipped with an 11.74 T wide-bore magnet. The samples were packed under argon atmosphere into cylindrical zirconia rotors with a diameter of 2.5 mm. The magic angle was calibrated using the ^{23}Na resonance of solid $NaNO_3$. Single-pulse MAS experiments were conducted using a 90° radio-frequency pulse of 3.15 μs at 120 W and a recycle delay of 15 s, with a spinning frequency of ν_{MAS} = 25.0 kHz. Chemical shifts for ^{23}Na were referenced to a freshly prepared 1 M NaCl aqueous solution at 0 ppm. Spectral fitting and analysis were performed using the ssNake software package.[43]

Static variable-temperature ^{23}Na saturation-recovery experiments were conducted in a VTN broadband probe at 4.7 T on a Bruker NEO 200 spectrometer with ν_0 = 52.94 MHz. For 90° rf pulses a pulse length of 3.4 μs at 120 W was used. Recycle delays were incremented from 10 μs up to maximum 10 s with four logarithmic steps per decade or stopped reaching a plateau.

The samples were packed under argon atmosphere into 4 mm cylindrical zirconia rotors. The temperature-dependent experiments were performed in a range from 250 K to 450 K with a step size of 10 K. An Air Jet XR compressor-based cooling system from SP Scientific (FTS System) in conjunction with an electrical heating system utilizing dried, compressed air was used for temperature regulation in the temperature range of 250 K to 290 K. For temperatures above 290 K only the electric heating and a dried, compressed air flow was used. The temperatures were calibrated using the known ^{1}H chemical shift temperature dependencies of methanol (250-290 K) and ethylene glycol (300-450 K).

Density functional Theory (DFT). To model local structure in the $NaTaO_xCl_{6-2x}$ family, we employed ab initio random structure searching (AIRSS)[44],[45] to generate candidate configurations capable of representing the diverse local structural environments arising from the absence of long-range order. Searches were performed for compositions x = 0, 0.5 and 1, corresponding to $NaTaCl_6$, $NaTaO_{0.5}Cl_{5.0}$, and $NaTaOCl_4$ respectively, to investigate the loss and partial recovery of long-range order as x increases from 0 to 1. Supercells containing 8, 16 and 32 atoms ($NaTaCl_6$),15, 30, and 45 atoms ($NaTaO_{0.5}Cl_{5.0}$) and 7, 14, and 28 atoms ($NaTaOCl_4$) were considered.

All candidate structures were relaxed using density functional theory (DFT) as implemented in the Vienna Ab initio Simulation Package (VASP).[46],[47],[48],[49] The choice of exchange–correlation functional and dispersion correction scheme was guided by a benchmarking study on representative compounds ($NaTaCl_6$ ($P2_1/n$, ICSD #36519)[50], $TaCl_5$ (C2/m, ICSD #409433)[51], $NaTaO_3$ (Pnma, ICSD #88375)[52] and $TaOCl_3$ (mp-1208583). The Perdew-Burke-Ernzerhof (PBE) functional[53] with D4 dispersion correction[54] yielded the best overall agreement with reference lattice parameters from the Inorganic Crystal Structure Database (ICSD) [55] and the Materials Project[56], and was therefore adopted for all subsequent calculations.

Projector augmented-wave (PAW) pseudopotentials[47] were used to describe the electron-ion interactions, with the following valence electron configurations: Na ($2p^6\ 3s^1$), Ta ($5p^6\ 5d^3\ 6s^2$), O ($2s^2\ 2p^4$), and Cl ($3s^2\ 3p^5$). A plane-wave kinetic energy cutoff of 624 eV was employed, as determined from convergence testing on the endpoint compounds. Brillouin zone integrations were performed on a Monkhorst-Pack mesh with a density of 0.327 $Å^{-1}$ mesh[57] for primitive cells. Electronic self-consistency was achieved using a convergence threshold of 1 x 10^{-6} eV

on the total energy, and ionic relaxations were performed until forces on all atoms were below [0.01 eV/Å].

Sodium-ion diffusion was investigated using *ab initio* molecular dynamics (AIMD). Calculations employed a Γ-only k-point mesh to reduce computational cost. Each structure was first relaxed to provide the starting configuration for AIMD. Simulations began with a 2 ps equilibration phase at 600 K, with a timestep of 2 fs and periodic velocity rescaling applied every 50 steps to maintain the target temperature. Following this, the system was equilibrated for an additional 2 ps in the canonical (NVT) ensemble with a Nosé-Hoover thermostat[58],[59] for temperature control. Production runs were then performed in the NVT ensemble at 600 K for 80 ps.

All calculation analyses were carried out using Python-based workflows, making use of the pymatgen[60], NumPy[61], SciPy[62], and kinisi[63],[64], ASE[65] Crystal torture[66] and dscribe[67] packages. OVITO[68] was used for visualization of molecular dynamics. Hofmann was used for all structural models[69].

Electrochemical Impedance Spectroscopy (EIS). Temperature-dependent electrochemical impedance spectroscopy was performed to determine the ionic conductivities and activation energies of the samples. Approximately 250 mg of each sample was pelletized by uniaxial pressing, followed by isostatic pressing for 1 h under 330 kN (~410 MPa). The resulting pellets had a thickness of approximately 0.1 cm and a diameter of about 0.9 cm. Both pellet faces were sputtered with a thin gold layer of ≈ 120 nm thickness using a Cressington Coating System 108a (40 mA, 300 s) to serve as electrodes. Pouch cells were fabricated by sealing the pellets in pouch foil, with aluminum tabs attached on each side acting as electrical contacts.

Impedance measurements were carried out using a Novocontrol system equipped with an Alpha Analyzer and a Quatro Cryosystem. Spectra were collected over a frequency range of 50 mHz to 10 MHz with an applied AC amplitude of 30 mV, at temperatures ranging from 173.15 K to 333.15 K. Data analysis was performed using RelaxIS 3 software (rhd instruments).

Quasielastic Neutron Scattering (QENS). QENS data for $x = 0.5$ was collected at the BASIS backscattering spectrometer at the Spallation Neutron Source, Oak Ridge National Laboratory.[70],[71] The Si (111) analyzers, operated with a neutron wavelength of 6.4 Å and a 60 Hz chopper frequency was selected. Approximately 5 g of sample was loaded into an aluminum sample holder consisting of a 1 mm-spaced double-wall cylinder, sealed with aluminum foil acting as a gasket. Measurements were performed at 100 K, 300 K, 325 K, and

350 K for about 5 hours each and temperature was controlled by using a closed-cycle refrigerator with a hot stage. Data reduction was performed using the Mantid software package, with normalization to a vanadium standard. The scattering data were binned into Q intervals of 0.2 $Å^{-1}$ width over the range 0.2 – 2.0 $Å^{-1}$, and energy intervals of 0.4 μeV width over −100 to 100 μeV. Data fitting was carried out using the Dave software package, employing the following model:

$$S(Q, E) = \left(A\delta(E) + B\frac{\pi\Gamma(Q)}{\Gamma(Q)^2 + E^2} \right) \cdot R(Q, E) + C(Q, E)$$

Here, $A\delta$ (E) represents the elastic scattering contribution, while the Lorentzian term accounts for the quasielastic broadening. Both are convoluted with the instrumental resolution function R (Q, E), approximated by the diffusion-less signal measured at 100 K. The term C (Q, E) describes a linear background function. From the Lorentzian fits, the half-width at half-maximum Γ (Q) of the quasielastic broadening was extracted. The Q-dependence of Γ (Q) was modeled using the Chudley-Elliott jump diffusion model to obtain jump distances and mean residence times, which were subsequently used to calculate diffusion coefficients at each temperature.[72]

Assembly and test of solid-state batteries. Solid-state cells were assembled using $Na_{0.67}Ni_{1/3}Fe_{1/3}Mn_{1/3}O_2$ (NFM) as the cathode active materials, $NaTaO_{0.5}Cl_{5.0}$ as the catholyte, and carbon nanofibers (CNF, Sigma-Aldrich) as a conductive additive, $Na_2(B_{10}H_{10})_{0.5}(B_{12}H_{12})_{0.5}$ as the separator and $Na_{2.25}Sn$ alloy as anode. The cathode composite consisting of 67% NFM, 31% $NaTaO_{0.5}Cl_{5.0}$ and 2% CNF by weight was homogenized using an egg-shaking process at 15 Hz for 15 minutes. $Na_{2.25}Sn$[73] and $Na(B_{10}H_{10})_{0.5}(B_{12}H_{12})_{0.5}$[74] were prepared using as described previously. The NFM was prepared using a coprecipitation method.[75]

The separator (~50 mg) was compacted in a PEEK-lined press cell equipped with stainless steel stamps acting as current collectors, using a uniaxial pressure of 3 tons applied for 3 minutes (~290 MPa). Following this, the press cell was opened on one side to insert the cathode composite (~11.7 mg, equivalent to an active material mass loading of 7.89 $mg \cdot cm^{-2}$), which was pressed onto the separator under identical conditions. The anode (~20 mg) was similarly applied to the opposite side and the full set up was pressed at 3 tons for 3 minutes. The cell was mechanically stabilized using a torque frame tightened to 10 Nm, corresponding to an estimated pressure of ~40 MPa. Electrochemical cycling was performed at room temperature (298.15 K). For long cycling the cells were conducted at a rate of 0.1 C, while for the rate tests after 5 cycles the rate was changed with an initial C-rate of 0.1 C, followed by 0.2 C, 0.5 C,

1 C (equivalent to a current density of 0.122 $mA \cdot cm^{-2}$, 0.244 $mA \cdot cm^{-2}$, 0.609 $mA \cdot cm^{-2}$ and 1.218 $mA \cdot cm^{-2}$, respectively) and 0.1 C as a repetition at the end. The cells were cycled within a voltage window of 2.2 to 3.4 V vs. Na/Na–Sn.

Author Information

Corresponding Authors

Wolfgang G. Zeier − Institute of Inorganic and Analytical Chemistry, University of Münster, 48149 Münster, Germany; Institut für Energiespeicher, IMD-4: Helmholtz-Institut Münster, Forschungszentrum Jülich,48149 Münster, Germany; orcid.org/0000-0001-7749-5089; Email: w.zeier@uni-muenster.de

Alexander G. Squires − School of Chemistry, University of Birmingham, Edgbaston, Birmingham B15 2TT, United Kingdom; orcid.org/0000-0001-6967-3690; Email: a.squires@bham.ac.uk

Authors

Justin Leifeld − Institut für Energiespeicher, IMD-4: Helmholtz-Institut Münster, Forschungszentrum Jülich, 48149 Münster, Germany; orcid.org/0009-0004-5237-0174

Abigail C. Parsons − School of Chemistry, University of Birmingham, Edgbaston, Birmingham B15 2TT, United Kingdom; orcid.org/0009-0007-9459-5509

Alexandra Morscher − Institute of Inorganic and Analytical Chemistry, University of Münster, 48149 Münster, Germany; orcid.org/0000-0001-9850-1222

Xabier Martinez de Irujo-Labalde − Institute of Inorganic and Analytical Chemistry, University of Münster, 48149 Münster, Germany; orcid.org/0000-0002-8759-4221

Marvin A. Kraft − Institut für Energiespeicher, IMD-4: Helmholtz-Institut Münster, Forschungszentrum Jülich, 48149 Münster, Germany; Institute of Inorganic and Analytical Chemistry, University of Münster, 48149 Münster, Germany; orcid.org/ 0009-0005-5632-4228

Oskar G. Soulas − School of Chemistry, University of Birmingham, Edgbaston, Birmingham B15 2TT, United Kingdom; orcid.org/0009-0003-1376-945X

Bibek Samanta − International Graduate School of Battery Chemistry, Characterization, Analysis, Recycling and Application (BACCARA) and Institute of Physical Chemistry, University of Münster, 48149 Münster, Germany; orcid.org/0000-0003-2177-5430

Wiebke Zielasko − Institute of Physical Chemistry, University of Münster, 48149 Münster, Germany

Neelam Yadav – Department of Chemistry, Humboldt-University Berlin, 10117 Berlin, Germany; Joint Research Operando Group Battery Analysis (CE-GOBA) Helmholtz-Zentrum Berlin für Materialien und Energie (HZB), 12489 Berlin, Germany; orcid.org/0000-0001-8633-7277

Kyra Strotmann − Institute of Inorganic and Analytical Chemistry, University of Münster, 48149 Münster, Germany

Niina Jalarvo − Neutron Scattering Division, Oak Ridge National Laboratory, Oak Ridge, Tennessee 37830, United States; orcid.org/0000-0003-0644-6866

Bruno V. M. Rodrigues – Chair of Inorganic Chemistry, Faculty of Mathematics and Natural Sciences, University of Wuppertal, 42119 Wuppertal, Germany; orcid.org/0000-0002-0130-8029

Adam Slabon – Chair of Inorganic Chemistry, Faculty of Mathematics and Natural Sciences, University of Wuppertal, 42119 Wuppertal, Germany; orcid.org/0000-0002-4452-1831

Philipp Adelhelm – Department of Chemistry, Humboldt-University Berlin, 10117 Berlin, Germany; Joint Research Operando Group Battery Analysis (CE-GOBA) Helmholtz-Zentrum Berlin für Materialien und Energie (HZB), 12489 Berlin, Germany; orcid.org/0000-0003-2439-8802

Michael Ryan Hansen − Institute of Physical Chemistry, University of Münster, 48149 Münster, Germany; orcid.org/0000-0001-7114-8051

David O. Scanlon − School of Chemistry, University of Birmingham, Edgbaston, Birmingham B15 2TT, United Kingdom; orcid.org/0000-0001-9174-8601

Notes

The authors declare no competing financial interest.

Acknowledgement

DOS gratefully acknowledges illuminating conversations with Professor Vladan Stevanovic on modelling amorphous materials. This work was funded by the Federal Ministry for Research, Technology and Space (BMFTR) under the project HiPoBat: High Power Batteries (FKZ: 13XP0611A). This research used resources at the Spallation Neutron Source, a DOE Office of Science User Facility operated by the Oak Ridge National Laboratory. The beamtime was allocated to BASIS on proposal number IPTS-35994. This study is funded by the European Union (ERC, DIONISOS, 101123802). Views and opinions expressed are however those of the author(s) only and do not necessarily reflect those of the European Union or the European Research Council Executive Agency. Neither the European Union nor the granting authority can be held responsible for them. Furthermore, would like to thank the University of Wuppertal for the research support and the DELTA synchrotron (Dortmund, Germany) for the beam time provided. University of Birmingham's BlueBEAR HPC service, the Baskerville Tier 2 HPC

service (https://www.baskerville.ac.uk/; funded by the EPSRC and UKRI through the World Class Labs scheme (EP/T022221/1) and the Digital Research Infrastructure programme (EP/W032244/1)), and the Sulis Tier 2 HPC platform hosted by the Scientific Computing Research Technology Platform at the University of Warwick (funded by EPSRC Grant EP/T022108/1 and the HPC Midlands+ consortium). Through our membership of the UK's HEC Materials Chemistry Consortium, which is funded by the UK Engineering and Physical Sciences Research Council (EPSRC; EP/L000202, EP/R029431, EP/T022213), this work also used ARCHER2 UK National Supercomputing Services. We are also grateful to the UK Materials and Molecular Modelling Hub for computational resources, which is partially funded by EPSRC (EP/T022213/1, EP/W032260/1 and EP/P020194/1). We would also like to thank M.R.H. and B.S. who carried out NMR-measurements and are members of the International Graduate School for Battery Chemistry, Characterization, Analysis, Recycling and Application (BACCARA), which is funded by the Ministry of Culture and Science of the State of North Rhine Westphalia, Germany.

References

[1] H. S. Hirsh, Y. Li, D. H. S. Tan, M. Zhang, E. Zhao, Y. S. Meng, *Advanced Energy Materials* **2020**, *10*.
[2] J. Huang, K. Wu, G. Xu, M. Wu, S. Dou, C. Wu, *Chemical Society reviews* **2023**, *52*, 4933.
[3] S. Ohno, W. G. Zeier, *Nat Energy* **2022**, *7*, 686.
[4] J. Janek, W. G. Zeier, *Nat Energy* **2016**, *1*.
[5] J. Janek, W. G. Zeier, *Nat Energy* **2023**, *8*, 230.
[6] F. Zheng, M. Kotobuki, S. Song, M. O. Lai, L. Lu, *Journal of Power Sources* **2018**, *389*, 198.
[7] J. A. Newnham, A. G. Squires, M. A. Kraft, D. O. Scanlon, W. G. Zeier, *Advanced Energy Materials* **2025**.
[8] S. Kmiec, E. Ruoff, A. Manthiram, *Angewandte Chemie (International ed. in English)* **2025**, *64*, e202416979.
[9] X. Martinez de Irujo-Labalde, T. Zhao, B. Samanta, T. Bernges, V. Faka, A. N. Sobolev, O. Maus, M. Appel, M. A. Kraft, M. R. Hansen et al., *J. Mater. Chem. A* **2024**, *12*, 33707.
[10] Z. Huang, S. Yoshida, H. Akamatsu, K. Hayashi, S. Ohno, *ACS Materials Lett.* **2024**, *6*, 1732.
[11] Y. Hu, J. Fu, J. Xu, J. Luo, F. Zhao, H. Su, Y. Liu, X. Lin, W. Li, J. T. Kim et al., *Matter* **2024**, *7*, 1018.
[12] T. Zhao, B. Samanta, X. M. de Irujo-Labalde, G. Whang, N. Yadav, M. A. Kraft, P. Adelhelm, M. R. Hansen, W. G. Zeier, *ACS Materials Lett.* **2024**, *6*, 3683.
[13] L. Zhou, J. D. Bazak, C. Li, L. F. Nazar, *ACS Energy Lett.* **2024**, *9*, 4093.

[14] Z. Huang, N. Yadav, S. Itakura, P. Song, H. Akamatsu, K. Hayashi, P. Gorai, S. Ohno, *Journal of the American Chemical Society* **2025**.
[15] E. B. Jones, V. Stevanović, *npj Comput Mater* **2020**, *6*, 56.
[16] L. Wolf, A. Novick, V. Stevanović, *Journal of Applied Physics* **2025**, *137*.
[17] E. Fransson, M. Slabanja, P. Erhart, G. Wahnström, *Advcd Theory and Sims* **2021**, *4*.
[18] E. Berger, E. Fransson, F. Eriksson, E. Lindgren, G. Wahnström, T. H. Rod, P. Erhart, *Computer Physics Communications* **2025**, *316*, 109759.
[19] B. Singh, Y. Wang, J. Liu, J. D. Bazak, A. Shyamsunder, L. F. Nazar, *Journal of the American Chemical Society* **2024**, *146*, 17158.
[20] P. Heitjans, M. Wilkening, *MRS Bull.* **2009**, *34*, 915.
[21] X. Wang, S. Zhang, J. Yue, X. Wang, Y. Xu, Y. Gong, L. Zhou, C. Zhao, J. Liang, X. Zhu et al., *Energy Environ. Sci.* **2025**, *18*, 9927.
[22] A. P. Bartók, R. Kondor, G. Csányi, *Phys. Rev. B* **2013**, *87*.
[23] Y. Wang, H. Huang, C. Rudin, Y. Shaposhnik, *Journal of Machine Learning Research* **2021**, 1.
[24] J. A. Newnham, J. Kondek, J. Hartel, C. Rosenbach, C. Li, V. Faka, L. Gronych, D. Glikman, F. Schreiner, D. D. Wind et al., *Chem. Mater.* **2025**, *37*, 4130.
[25] J. A. S. Oh, Z. Yu, C.-J. Huang, P. Ridley, A. Liu, T. Zhang, B. J. Hwang, K. J. Griffith, S. P. Ong, Y. S. Meng, *Joule* **2025**, *9*, 102130.
[26] B. Wankmiller, M. R. Hansen, *Journal of Magnetic Resonance Open* **2023**, *14-15*, 100098.
[27] A. Kuhn, M. Kunze, P. Sreeraj, H. D. Wiemhöfer, V. Thangadurai, M. Wilkening, P. Heitjans, *Solid state nuclear magnetic resonance* **2012**, *42*, 2.
[28] S. Lunghammer, D. Prutsch, S. Breuer, D. Rettenwander, I. Hanzu, Q. Ma, F. Tietz, H. M. R. Wilkening, *Scientific reports* **2018**, *8*, 11970.
[29] M. Uitz, V. Epp, P. Bottke, M. Wilkening, *J Electroceram* **2017**, *38*, 142.
[30] M. Yang, Z. Fan, J. Liu, Y. Ma, Y. Bai, X. Wang, H. Zhang, F. Hai, W. Hua, Y. Ma et al., *Energy Fuels* **2024**, *38*, 2453.
[31] E. Schlautmann, J. Drews, L. Ketter, M. A. Lange, T. Danner, A. Latz, W. G. Zeier, *ACS Energy Lett.* **2025**, *10*, 1664.
[32] L. Ketter, N. Greb, T. Bernges, W. G. Zeier, *Nature communications* **2025**, *16*, 1411.
[33] E. Schlautmann, A. Weiß, O. Maus, L. Ketter, M. Rana, S. Puls, V. Nickel, C. Gabbey, C. Hartnig, A. Bielefeld et al., *Advanced Energy Materials* **2023**, *13*.
[34] R. Tian, S.-H. Park, P. J. King, G. Cunningham, J. Coelho, V. Nicolosi, J. N. Coleman, *Nature communications* **2019**, *10*, 1933.
[35] T. Bernges, L. Ketter, B. Helm, M. A. Kraft, K. A. See, W. G. Zeier, *EES Batteries* **2025**, *1*, 172.
[36] K. Jun, Y. Sun, Y. Xiao, Y. Zeng, R. Kim, H. Kim, L. J. Miara, D. Im, Y. Wang, G. Ceder, *Nature materials* **2022**, *21*, 924.
[37] K. Jun, G. Wei, X. Yang, Y. Chen, G. Ceder, *Matter* **2025**, *8*, 102001.
[38] P. Thompson, D. E. Cox, J. B. Hastings, *J Appl Crystallogr* **1987**, *20*, 79.
[39] S. L. J. Thomae, N. Prinz, T. Hartmann, M. Teck, S. Correll, M. Zobel, *The Review of scientific instruments* **2019**, *90*, 43905.
[40] P. Juhas, T. Davis, C. L. Farrowa, S. J. L. Billinge, *PDFgetX3: a rapid and highly automatable program for processing powder diffraction data into total scattering pair distribution functions*, **2013**.

[41] D. Lützenkirchen-Hecht, R. Wagner, S. Szillat, A. K. Hüsecken, K. Istomin, U. Pietsch, R. Frahm, *Journal of synchrotron radiation* **2014**, *21*, 819.
[42] B. Ravel, M. Newville, *Journal of synchrotron radiation* **2005**, *12*, 537.
[43] S. G. J. van Meerten, W. M. J. Franssen, A. P. M. Kentgens, *Journal of magnetic resonance (San Diego, Calif. : 1997)* **2019**, *301*, 56.
[44] C. J. Pickard, R. J. Needs, *Journal of physics. Condensed matter : an Institute of Physics journal* **2011**, *23*, 53201.
[45] C. J. Pickard, R. J. Needs, *Physical review letters* **2006**, *97*, 45504.
[46] G. Kresse, J. Furthmüller, *Computational Materials Science* **1996**, *6*, 15.
[47] G. Kresse, D. Joubert, *Physical review. B, Condensed matter* **1999**, *59*, 1758.
[48] G. Kresse, J. Furthmüller, *Physical review. B, Condensed matter* **1996**, *54*, 11169.
[49] G. Kresse, J. Hafner, *Physical review. B, Condensed matter* **1993**, *47*, 558.
[50] H. Henke, *Zeitschrift für Kristallographie* **1992**, *198*, 1.
[51] S. Rabe, U. Müller, *Zeitschrift für Kristallographie - New Crystal Structures* **2000**, *215*, 1.
[52] B. J. Kennedy, A. K. Prodjosantoso, C. J. Howard, *Journal of physics. Condensed matter : an Institute of Physics journal* **1999**, *11*, 6319.
[53] J. P. Perdew, K. Burke, M. Ernzerhof, *Physical review letters* **1997**, *78*, 1396.
[54] E. Caldeweyher, S. Ehlert, A. Hansen, H. Neugebauer, S. Spicher, C. Bannwarth, S. Grimme, *The Journal of chemical physics* **2019**, *150*, 154122.
[55] D. Zagorac, H. Müller, S. Ruehl, J. Zagorac, S. Rehme, *J Appl Crystallogr* **2019**, *52*, 918.
[56] A. Jain, S. P. Ong, G. Hautier, W. Chen, W. D. Richards, S. Dacek, S. Cholia, D. Gunter, D. Skinner, G. Ceder et al., *APL Materials* **2013**, *1*.
[57] H. J. Monkhorst, J. D. Pack, *Phys. Rev. B* **1976**, *13*, 5188.
[58] S. Nosé, *The Journal of chemical physics* **1984**, *81*, 511.
[59] W. G. Hoover, *Physical review. A, General physics* **1985**, *31*, 1695.
[60] S. P. Ong, W. D. Richards, A. Jain, G. Hautier, M. Kocher, S. Cholia, D. Gunter, V. L. Chevrier, K. A. Persson, G. Ceder, *Computational Materials Science* **2013**, *68*, 314.
[61] C. R. Harris, K. J. Millman, S. J. van der Walt, R. Gommers, P. Virtanen, D. Cournapeau, E. Wieser, J. Taylor, S. Berg, N. J. Smith et al., *Nature* **2020**, *585*, 357.
[62] P. Virtanen, R. Gommers, T. E. Oliphant, M. Haberland, T. Reddy, D. Cournapeau, E. Burovski, P. Peterson, W. Weckesser, J. Bright et al., *Nature methods* **2020**, *17*, 261.
[63] A. R. McCluskey, A. G. Squires, J. Dunn, S. W. Coles, B. J. Morgan, *JOSS* **2024**, *9*, 5984.
[64] A. R. McCluskey, S. W. Coles, B. J. Morgan, *Journal of chemical theory and computation* **2025**, *21*, 79.
[65] A. Hjorth Larsen, J. Jørgen Mortensen, J. Blomqvist, I. E. Castelli, R. Christensen, M. Dułak, J. Friis, M. N. Groves, B. Hammer, C. Hargus et al., *Journal of physics. Condensed matter : an Institute of Physics journal* **2017**, *29*, 273002.
[66] C. O'Rourke, B. Morgan, *JOSS* **2019**, *4*, 1306.
[67] L. Himanen, M. O. Jäger, E. V. Morooka, F. Federici Canova, Y. S. Ranawat, D. Z. Gao, P. Rinke, A. S. Foster, *Computer Physics Communications* **2020**, *247*, 106949.
[68] A. Stukowski, *Modelling Simul. Mater. Sci. Eng.* **2010**, *18*, 15012.
[69] B. J. Morgan, "hofmann. A modern Python reimagining of the XBS ball-and-stick crystal structure viewer.", zu finden unter https://github.com/bjmorgan/hofmann.

[70] E. Mamontov, K. W. Herwig, *The Review of scientific instruments* **2011**, *82*, 85109.
[71] N. C. Osti, N. Jalarvo, E. Mamontov, *Materials horizons* **2024**, *11*, 4535.
[72] C. T. Chudley, R. J. Elliott, *Proc. Phys. Soc.* **1961**, *77*, 353.
[73] L. E. Goodwin, P. Till, M. Bhardwaj, N. Nazer, P. Adelhelm, F. Tietz, W. G. Zeier, F. H. Richter, J. Janek, *ACS applied materials & interfaces* **2023**, *15*, 50457.
[74] M. Brighi, F. Murgia, Z. Łodziana, P. Schouwink, A. Wołczyk, R. Cerny, *Journal of Power Sources* **2018**, *404*, 7.
[75] X. Wen, C. Yang, Z. Fang, C. Zhong, J. Ou, *Chemical Engineering Journal* **2025**, *522*, 167832.